Prediction of Atmospheric Noise Temperature at the Deep Space Network with Machine Learning

Longtao Wu[1], David D. Morabito[1], Joaquim P. Teixeira[1], Lei Huang[1*], Hai M. Nguyen[1], Hui Su[1], Melissa A. Soriano[1], Lei Pan[1], and Daniel S. Kahan[1]

[1]Jet Propulsion Laboratory, California Institute of Technology, Pasadena, California, USA.

*Now at University of California, Los Angeles.

Corresponding author: Longtao Wu (longtao.wu@jpl.nasa.gov)

Key Points:

- A customized real-time weather forecast system is developed for the Deep Space Network tracking sites using a machine learning method.
- 90% of the 24-hour forecasted atmospheric noise temperature has root-mean-squared-error less than 3.50 K.
- Up to 45% more data can be realized for Ka-band communications links using the real-time weather forecast system.

Abstract

Ka-band (32 GHz) communications links utilized by the National Aeronautics and Space Administration (NASA) flight missions for science downlink are susceptible to degradation due to weather. In this study, a customized real-time forecast system has been developed to predict zenith atmospheric noise temperature (T_{atm}) at the Deep Space Network (DSN) tracking sites using machine learning (ML). A random forest model is trained with the Global Forecast System (GFS) forecast and analysis datasets in addition to the T_{atm} measurements derived from on-site advanced water vapor radiometers (AWVR). The real-time forecast uncertainty is quantified for different error regimes using the Self-Organizing Map method.

The results show that the Root Mean Square Error (RMSE) of the 24-hour T_{atm} prediction at Goldstone, CA increases with the increase of T_{atm}. Ninety percent of the forecasts have RMSE (bias) of less than 3.50 K (0.22 K) for fair-weather conditions with $T_{atm} < 17$ K. In comparison to the current approach in designing Ka-band communications links, application of weather forecasts can increase data return to the downlink for 80% of the time. A downlink gain of up to 1.61 dB (45% more data) can be realized at 20° elevation angle when $T_{atm} = 9$ K.

1 Introduction

Ka-band (32 GHz) communications links utilized by the National Aeronautics and Space Administration (NASA) deep space flight missions for science downlink are more susceptible to degradation due to weather than lower frequency S-band (2.3 GHz) and X-band (8.4 GHz) (Slobin, 2009). The current approach in designing Ka-band communications links employs conservative assumptions, such as designing at the lowest elevation angle of a tracking pass and with high probability of weather constraints (Davarian et al., 2004). For example, the Europa Clipper mission assumes a 3 dB margin for the data downlink. Such assumptions can result in inefficient downlink capacity. By making use of real-time weather forecasting one can greatly increase data return efficiency and the reliability of the communications links (Shambayati, 2004; Biscarini et al., 2016; Morabito et al., 2016; Nikoukar et al., 2020).

Weather service agencies, such as the National Centers for Environmental Prediction (NCEP), provide operational weather forecasts globally using numerical weather prediction (NWP) models. Raw NWP output, however, is not adequate to resolve the fine-scale topographical features and mesoscale processes that govern local weather at specific locations, such as at the Deep Space Network (DSN) tracking sites. In addition, the NWP raw output contains biases relative to local observations. Morabito et al. (2016) showed that the NWP model captures local weather conditions at the DSN tracking sites most of time but significant discrepancies occur due to cloud and precipitation processes.

A variety of (dynamical or statistical) downscaling methods have been developed to provide robust weather predictions at local scales for various applications (Barsugli et al., 2013). Dynamical downscaling extrapolates the effects of large-scale processes to regional or local scales of interest using high-resolution NWP models. Physical laws are explicitly represented in the NWP models. However, dynamical downscaling can be sensitive to biases in the boundary and initial conditions from large-scale coarse-resolution models. Dynamical downscaling can be computationally expensive, which is not practical for use in mission operations such as for command and on-board control. Statistical downscaling determines relationships between large-scale patterns simulated by the global NWP models and responses on the local scale using statistics-based techniques, including Machine Learning (ML) methods. These relationships are applied to the NWP outputs and are transformed into statistical inferences of local responses with bias corrections. Statistical downscaling requires a relatively low number of computing resources and can be readily applied to real-time or near real-time space mission operations.

In this study, a customized weather forecast system with uncertainty quantification (UQ) is developed for the DSN tracking sites using a ML method. The workflow of the ML forecast system is shown in Figure 1. We use global NWP datasets and in-situ observations to train the ML-forecast model. A UQ model is also trained to characterize the bias and standard error of the real-time forecasts. Thus, real-time weather forecasts with error characteristics can be provided for the DSN tracking sites. More details of the real-time ML forecast system will be described in the following sections. We use a 24-hour forecast of zenith atmospheric noise temperature (T_{atm}) at Goldstone, CA as a demonstration case of the ML forecast system. This ML forecast system will be adopted to other tracking sites and expanded to predict other atmospheric variables when in-situ observations become available.

Section 2 describes the datasets used for the training and testing of the ML forecast system. The ML forecast model and the forecast results are presented in section 3. Section 4 presents the

UQ model and results. Section 5 discusses the assessments of the ML forecasts used to quantify improvements in Ka-band downlink efficiency for the Europa Clipper mission. Section 6 provides summary and discussion.

2 Training and testing datasets

2.1 Atmospheric noise temperature

This study aims to apply ML to NWP model forecast data and generate real-time forecasts of zenith T_{atm} at the DSN tracking sites, which can be ingested into the DSN communication link protocol. The increase of T_{atm} can be used to assess other weather-induced effects such as attenuation due to gas (e.g. water vapor and oxygen), cloud liquid and rain liquid (Slobin, 2009; Morabito, 2014). The Advanced Water Vapor Radiometer (AWVR) has been used to measure weather effects at the DSN Goldstone tracking site for over 20 years and at the Madrid site for ~11 years. The AWVRs were primarily developed to remove atmospheric effects from radio science data for the Cassini mission and are currently being used for the Juno mission (see references in Morabito et al., 2022). T_{atm} and precipitable water vapor (PWV) can be derived from sky brightness temperatures observed by the AWVR (Slobin, 2005; Morabito, 2007; Morabito et al., 2015; 2016; 2022). The AWVR data acquired in 2019 encountered problems related to inadequate temperature control (Morabito et al., 2022), thus these data are not used in this study.

We use hourly-averaged T_{atm} from 2015 to 2020 (except 2019) as observations to train and test the ML forecast system. The AWVR observations (Figure 2) show that the minimum value of T_{atm} at Goldstone is 7.15 K. The maximum value of T_{atm} can be up to 132.10 K (or higher), mainly due to the impacts of cloud liquid and rain precipitation. 90% (95%) of the T_{atm} observations are less than 16.50 K (19.11 K).

2.2 NWP analysis and forecast

NCEP Global Forecast System (GFS) provides global analysis and forecasts (up to 16 days) of the weather at 0.25° horizontal resolution every six hours (NCEP, 2015). The GFS data archive is available online with data spanning from 2015/01/15 to the present. Data samples numbering 5435 from both the GFS and AWVR are available to train and test the ML forecast model. Both GFS analyses and forecasts are used as predictors, in order to retain information from current observations and physical model forecasts.

We analyze the correlation of $\ln(T_{atm})$ at 24-hours after the forecasting time (T24) with the coarse-grid-scale variables from both GFS analysis and 24-hour forecasts at the forecasting time (T0). Figure 3 shows that GFS 24-hour forecast (PWV_f024) nicely predicts the magnitude and variation of PWV observed at Goldstone (PWV_AWVR) for year 2017. The variation of $\ln(T_{atm})$ is following the variation of PWV most of the time, with a correlation coefficient of 0.71 between the $\ln(T_{atm})$ at T24 and the 24-hour forecasted PWV at T0. In this study, those GFS variables with correlation > 0.30 are selected as the predictors to forecast $\ln(T_{atm})$ at T24 in the ML forecast model (Table 1). In general, GFS 24-hour forecasts have better correlation with T_{atm} than GFS analysis, because GFS 24-hour forecasts are valid at the same time of T_{atm} while GFS analysis is valid at 24 hours before T_{atm}. All of the moisture, cloud, precipitation and surface meteorological data from the 24-hour forecasts provide useful information to predict T_{atm}. Only PWV and surface meteorological data from analysis have correlation with $\ln(T_{atm})$ that are larger

than 0.30. This suggests that including NWP forecasts as predictors will provide better forecast skills than using in-situ measurements alone.

3 Machine learning forecast

Random forest (RF) regressor in the standard Python scikit-learn package (https://scikit-learn.org/stable/modules/generated/sklearn.ensemble.RandomForestRegressor.html) is used to build the ML-based forecast system. Historical AWVR and GFS data (a total of 5,435 samples) from 2015 to 2020, except 2019, are used for model training and testing. Pipeline in the scikit-learn package (https://scikit-learn.org/stable/modules/generated/sklearn.pipeline.Pipeline.html) is applied for the standardization of the predictors. Hyperparameters are optimized by a grid search with the 10-fold cross-validation method (https://scikit-learn.org/stable/modules/generated/sklearn.model_selection.GridSearchCV.html). Model performance is evaluated by inspecting the root mean square error (RMSE) of T_{atm} relative to the AWVR measurements. We evaluate the model performance using the "leave-one-year-out" cross validation method (Kaplan et al., 2015; Su et al., 2020), which ensures the independence of the training and testing data. That is, for a single model, four years' worth of data are used to train the ML forecast model and the withheld year is used to evaluate the forecast performance.

The forecasted T_{atm} has a similar distribution to that of the AWVR observations (Figure 2). However, the data range in the forecast is smaller than that of the observations. The minimum (maximum) value is 7.80 K (43.19 K) in the forecast vs. 7.15 K (132.10 K) in the AWVR observation. Figure 4 shows that the forecasted T_{atm} has good agreement with the observations, especially when the observed T_{atm} is less than 17 K. The RMSE (bias) of all of the forecasts is 4.72 (−0.27) K. Ninety percent of the forecast T_{atm} has a bias within 0.25 K (Figure 5a). The RMSE for T_{atm} < 9.50 K (20% of the forecasted T_{atm}) is 0.63 K (Figure 5b). The RMSE increases with the increase of T_{atm}. Ninety percent of the forecasts has a RMSE less than 3.50 K (or 25% relative to the mean T_{atm}) for fair-weather conditions with T_{atm} < 17 K. The forecast RMSE increases significantly for extreme-weather conditions with T_{atm} > 17 K.

The PWV_f024 from GFS is the most important predictor of T_{atm} in the RF forecast model (Figure 6), consistent with the highest correlation between PWV_f024 and $\ln(T_{atm})$ (Table 1). The 24-hour forecasts from GFS are more important than the analysis from GFS in the RF forecast model, consistent with the correlations in Table 1. The relative importance of predictors are similar in different years with slight differences in the magnitude of the relative importance.

4 Uncertainty quantification (UQ)

Real-time error characterization is provided by a UQ methodology similar to that in Teixeira et al. (2021), wherein a clustering algorithm is used to identify regimes of prediction error. Teixeira et al. (2021) showed that error characterization of a geophysical prediction of atmospheric motion vectors benefitted from separating those predictions into different geophysical regimes because the error characteristics of the predictions can vary significantly between the regimes. The cursory analysis (Figure 5) shows that the bias and RMSE of the RF prediction is significantly greater for predictions of T_{atm} > 17 K. We enhance upon this simple observation by clustering with predictor variables in addition to the predictions themselves in the UQ analysis.

A schematic of our UQ approach is detailed in Figure 7. We denote the predictors of the RF model as X, the RF prediction as $\hat{Y}$, and the observed T_{atm} as Y. We characterize the error as

both bias (the mean of $[\widehat{\mathrm{Y}} - \mathrm{Y}]$) and standard error (the standard deviation of $[\widehat{\mathrm{Y}} - \mathrm{Y}]$). After randomly splitting the dataset into a training (75%) and a testing (25%) set, we first train a clustering algorithm (a self-organizing map [SOM], as will be discussed in a subsequent paragraph) on the set of predictors X, predictions $\widehat{\mathrm{Y}}$, and observations Y from the training dataset (Panel 1 in Figure 7). Because it includes both the RF prediction and the observed T_{atm}, the clustering algorithm captures regimes of prediction error better than it would if the observed T_{atm} were not included. Of course, this implies a trade-off in which the clustering algorithm itself cannot be used operationally, since we have no knowledge of the actual T_{atm} in real applications; instead, we develop a classification algorithm (specifically a classification RF) which maps each set of predictors and prediction (X and $\widehat{\mathrm{Y}}$) to its assigned cluster (Panel 2 in Figure 7). As such, any RF prediction and its associated predictors can be assigned a set of probabilities of belonging to each cluster. Subsequently, the bias and standard error for a particular RF prediction is the weighted mean of the biases and standard errors from each of the clusters (when applied to the testing set), where each value is weighted by the probability mapped from the RF prediction to that respective cluster. Because the clustering approach can be sensitive to the initial conditions of the training dataset, we run an ensamble of 100 identical models with different randomly-sample training datasets. The final model is the mean across the ensamble of predicted bias and standard error values.

We employed a self-organizing map in the clustering portion of the error characterization model. SOM is an unsupervised learning technique in which a neural net fits a grid of neurons to the topological shape of a dataset. We choose SOM due to their repeated success in clustering atmospheric data into identifiable and interpretable geophysical regimes (Marques and Chen, 2003; Richardson et al., 2003; Liu et al., 2006). As in Teixeira et al. (2021), we validated our trained model using the Continuous Rank Probability Score (CRPS), a scoring rule for probabilistic forecasts. CRPS is as a function of a cumulative distribution function F and an observation $\boldsymbol{x}$ as follows:

$$\mathrm{CRPS}(\mathrm{F}, \mathbf{x}) = \int_{-\infty}^{\infty} (\mathrm{F}(\mathbf{y}) - \mathrm{H}(\mathbf{y} - \mathbf{x}))^2 \, \mathbf{dy}$$

where H() is the Heaviside step function (Gneiting and Katzfuss, 2014). In this context, F is the cumulative distribution function associated with the bias and standard error that the UQ model provides, while $\boldsymbol{x}$ is a scalar observation of the difference between T_{atm} and the model prediction. In essence, CRPS attempts to measure how close an observation is to the center of a distribution, while penalizing distributions that are unnecessarily wide. We analyze the mean CRPS value for the test population of T_{atm} errors, with a lower CRPS value reflecting a more calibrated probabilistic forecast. Conveniently, the CRPS also serve as a metric for selecting the optimal number of clusters for SOM. Figure 8 shows CRPS values evaluated under different choices of cluster number compared against the CRPS value for a naïve model, which is equivalent to a single-regime model in which the error distributions are given by the population mean and population standard deviation of T_{atm}. The figure illustrates two key observations. Firstly, for all SOMs, the CRPS of forecasts is significantly lower than that of the naïve model; secondly, that as the number of clusters increases, the CRPS decreases in a inverse-logarithmic fashion.

The second observation forms the basis for our choice of the cluster number. Our final model consists of SOM with a 30×30 feature grid which clusters the training data into 50 distinct

regimes. The UQ values applied on the testing dataset are illustrated in Figure 9. For 80% of the data, the estimated bias ranges between with −1.00 K and 1.76 K. However, for the 10% of data lying in the extremes, the estimated bias can range as low as −11.30 K and as high as 38.32 K. The RMSE estimates are similarly skewed: 50% of the data has an estimated RMSE estimate between 0.67 K and 1.99 K; a further 30% range between 2.00 K and 3.28 K; and the highest 20%, however, ranges between 3.28 K and 12.59 K.

We note that the results of the UQ analysis a bit different from that of Figure 5. Specifically, Figure 5 indicates that the first 40th percentile of data have a RMSE < 1.00 K, while the UQ result, as illustrated by the right-most panel of Figure 9, predicts that 40th percentile of data have a RMSE < 1.76 K. We note that this is because Figure 5 is derived from validation versus withheld data, and in general we would not know the prediction uncertainty of an estimate that arises from the forecast T_{atm} from the ML model in section 3. This gap is filled by the methodology in section 4, and the corresponding analog to Figure 5 is illustrated in the right panel of Figure 9. In general, the UQ methodology tends to overestimate the uncertainty of low T_{atm} percentiles, while underestimating the uncertainty of high T_{atm} percentiles. However, the similar upward convex shapes of the two plots and their similar magnitudes are encouraging, especially since estimation of uncertainties (second moments) tend to be much more difficult than estimation of the means (first moments).

5 Link budget analysis

The link budget analysis used by flight projects and telecom engineers makes use of the received signal-to-noise (SNR) as a key parameter related to data rate (Yuen, 1983). Received SNR is related to the received signal power divided by the observed noise power. The downlink signal power consists of contributions from the spacecraft transmit power, antenna gain, and various losses encountered as the signal propagates down to the receiving antenna, followed by contributions such as the gain of the receiving antenna. One of the loss contributors is due to the atmosphere, consisting primarily of the atmospheric attenuation due to oxygen and water vapor absorption, as well as liquid water such as in clouds and rain. Observed noise power includes the contribution due to the atmosphere, which is related to the elevation angle of the antenna, the optical depth of the atmosphere at zenith, and the effective radiating temperature of the atmosphere.

Telecom engineers typically use two types of SNR to analyze a link: carrier SNR and data channel SNR (we neglect ranging). For all link budgets, we ensure that the carrier SNR is adequate for signal lock. The data channel SNR is converted to the bit SNR (E_b/N_o) using the data rate. For a given elevation angle, we can define the downlink gain from the application of weather forecasts (forecast gain) as being the difference between the E_b/N_o using the forecast-provided zenith T_{atm} (adjusted to the elevation angle of interest) and the E_b/N_o using the nominal DSN Telecommunications Link Design handbook, 810-005 (Slobin, 2009) provided zenith value at 90% weather availability (and then adjusted to the elevation angle of interest).

The link budget approach made use of nominal Europa Clipper link budget parameters at Ka-band taken from the Europa Clipper Telecommunications Design Control Document (Babuscia et al., 2020). A link budget was first generated to verify agreement with Europa Clipper project Ka-band downlink link budget from Babuscia et al. (2020), which assumed a range distance of 6.4 AU, an elevation angle of 10º, no Jupiter hot-body noise and the Canberra, Australia DSN tracking site.

Next, the link budget was run to reference Goldstone as the downlink site using a Ka-band (32 GHz) capable downlink 34-m diameter antenna. The links were run with both the DSN Telecommunications Link Design handbook's assumptions and weather forecast assumptions provided by the forcasting results. We assumed no ranging in any of the links, just a carrier channel and a downlink data channel with Binary Phase-shift Keying (BPSK) modulation. The link budgets were run for elevation angles of 90º, 60º, 40º and 20º with zenith $T_{atm} \pm \sigma$ values of 8.96 ± 0.63 K, 10.02 ± 0.95 K, 11.10 ± 1.98 K, 12.75 ± 2.99 K, 14.57 ± 2.35 K, 15.76 ± 3.30 K, 17.57 ± 9.78 K and 22.55 ± 16.48 K. The results were examined and provided to the forecasting system.

The results of forecast gain versus mean T_{atm} is shown in Figure 10 for each elevation angle case. At the low-end of T_{atm} = 8.98 K, one can realize a forecast gain of 1.61 dB (45% more data) at 20° elevation angle with an uncertainty of 0.16 dB. This forecast gain is significant and would result in higher data return for missions with Ka-band telecommunication links. The forecast gain decreases with the increase of T_{atm}. At 80% of the time, higher data return can be realized when weather forecasting is used in telecommunication operations in place of using 90% weather availability in the link assumptions. All of the curves intersect at 0 dB for 15.76 K, as this is the 90% weather availability point to which projects nominally design. Below this point at the high-end of T_{atm}, most of the curves lie above the typical telecom link analysis margin point (–3 dB), implying that using 3 dB margin is adequate here. If a project opts to, they can lower the data rate appropriately during these adverse weather conditions to ensure lock-up with added margin.

6 Summary and discussion

In this study, we have developed a customized real-time weather forecast system for the DSN tracking sites using a ML method. A RF forecast model is trained using the global GFS forecast and analysis datasets and the T_{atm} derived from the AWVR measurements at Goldstone, CA. Twenty-four hour forecasts of T_{atm} are provided at Goldstone, CA. Error characterization of the forecasts is calculated using a SOM clustering and a RF classification method. Downlink gain of the telecommunications links is estimated by comparing the differences between using the real-time weather forecasts and using the 90% weather availability in a telecommunication link budget model.

The forecasts have a RMSE of 0.63 K for $T_{atm} < 9.50$ K. Forecast error increases when the T_{atm} increases. Ninety percent of the forecasts have a RMSE < 3.50 K and a bias within 0.25 K. The RMSE for all the forecasts is 4.72 K. The UQ methodology allows real-time ML forecasts to have unique RMSE values and bias estimates; 90% of forecasts will have an estimated RMSE < 4.49 K and an estimated bias within ± 2K. Forecast gain can be as high as 1.61 dB (45% more data downlink) when the forecasted T_{atm} is at the low-end at 20 deg elevation. Higher data return can be realized for 80% of the time if the real-time weather forecast is applied in flight project operations.

The real-time ML forecast system can provide forecasts of up to 16 days ahead for the DSN tracking sites. Real-time commands would be used to change data rates downlinked by the spacecraft for short time span forecasts (~6 hours to 2 days, which depends on round-trip light time and project operations). Forecasts over a longer time span may be used in the preparation of upcoming tracks such as defining data rate profiles in command loads that are uplinked to the spacecraft. For projects that uplink command loads on reasonably short periods such as within two weeks, these forecasts can be used to provide canned-in downlink rates to the uplink command loads. Real time commands would then be used to override these in case of significant weather

changes from the 16-day forecasts versus the 1-2 day forecasts. This ML forecast system will be adopted to other tracking sites and expanded to predict other atmospheric variables in future studies.

With enhancement of knowledge and advancement of technology, technical issues for deep space missions have become increasingly more complex and comprehensive. Larger volumes and more diverse types of data are and will be collected. As the capacity of on-board data storage becomes stressed, efficient transmission of data to Earth in a timely fashion is desired. The ML model for predicting T_{atm} can be generalized to many other missions in which data communications are essential. It could serve as a component of future onboard data prioritization protocol.

Acknowledgments

We would like to acknowledge Alan Tanner and Stephen Keihm for their methodological recommendations for calibration of the AWVR data. The research was carried out at the Jet Propulsion Laboratory, California Institute of Technology, under a contract with the National Aeronautics and Space Administration (80NM0018D0004).

References

Babuscia, A., M. Soriano, and P. Ilott (2020), Europa Clipper Telecommunications Design Control Document, Revision A, JPL D-101604, Jet Propulsion Laboratory, Pasadena, California, October 22, 2020.

Barsugli, J. J., Guentchev, G., Horton, R. M., Wood, A., Mearns, L. O., Liang, X.-Z., Winkler, J. A., Dixon, K., Hayhoe, K., Rood, R. B., Goddard, L., Ray, A., Buja, L., & Ammann, C. (2013). The practitioner's dilemma: How to assess the credibility of downscaled climate projections. Eos, Transactions American Geophysical Union, 94(46), 424–425. https://doi.org/10.1002/2013EO460005

Biscarini, M. et al. (2016), Optimizing data volume return for Ka-band deep space links exploiting short-term radiometeorological model forecast, *IEEE Trans. Antennas Propag.*, vol. 64, no. 1, pp. 235-250.

Gneiting, T. and M. Katzfuss (2014), Probabilistic forecasting, *Annu. Rev. Stat. Appl.*, 1, 125–151.

Kaplan, J., Rozoff, C. M., DeMaria, M., Sampson, C. R., Kossin, J. P., Velden, C. S., et al. (2015). Evaluating environmental impacts on tropical cyclone rapid intensification predictability utilizing statistical models. Weather and Forecasting, 30, 1374–1396. https://doi.org/10.1175/WAF-D-15-0032.1

Liu, Y., R. H. Weisberg and R. He (2006), Sea surface temperature patterns on the West Florida Shelf using the growing hierarchical self-organizing maps. *Journal of Atmospheric and Oceanic Technology*, Vol. No. 2, 23, 325-328, ISSN 0739-0572.

Marques, N. C. and N. Chen (2003), Border detection on remote sensing satellite data using self-organizing maps, *Proceedings of EPIA 2003 – 11th Portuguese conference on Artificial Intelligence*, pp. 294-307, ISBN 3-540-20589-6, Beja, Portugal, December 2003, Springer-Verlag, Berlin.

Morabito, D. D. (2014), A Comparison of Estimates of Atmospheric Effects on Signal Propagation Using ITU Models: Initial Study Results, *The Interplanetary Network Progress Report*, vol. 42-199, pp. 1–24. http://ipnpr.jpl.nasa.gov/progress_report/42-199/199D.pdf

Morabito, D. D., S. Keihm, and S. Slobin (2015), A Statistical Comparison of Meteorological Data Types Derived from Deep Space Network Water Vapor Radiometers, *The Interplanetary Network Progress Report*, vol. 42-203, pp. 1–21. http://ipnpr.jpl.nasa.gov/progress_report/42-203/203A.pdf

Morabito, D. D., L. Wu, and S. Slobin (2016), Weather Forecasting for Ka-band Operations: Initial Study Results, *The Interplanetary Network Progress Report*, vol. 42-206, pp. 1–24. https://ipnpr.jpl.nasa.gov/progress_report/42-206/206C.pdf

Morabito, D. D., D. Kahan, M. Paik, L. Wu, E. Barbinis, D. Buccino and M. Parisi (2022), A Study of Twenty Years of Advanced Water Vapor Radiometer Data at Goldstone, California, *The Interplanetary Network Progress Report*, vol. 42-228, pp. 1-18. https://ipnpr.jpl.nasa.gov/progress_report/42-228/42-228A.pdf

353 Nikoukar, R., D. Copeland, S. Sprouse, M. Cox and K. Kufahl (2020), Quantifying Weather
354 Effects on Ka-band Communication Links: A Parker Solar Probe Study, *2020 IEEE Aerospace*
355 *Conference*, 2020, pp. 1-9, doi: 10.1109/AERO47225.2020.9172786.

356 National Centers for Environmental Prediction/National Weather Service/NOAA/U.S.
357 Department of Commerce. 2015, updated daily. NCEP GFS 0.25 Degree Global Forecast Grids
358 Historical Archive. Research Data Archive at the National Center for Atmospheric Research,
359 Computational and Information Systems Laboratory. https://doi.org/10.5065/D65D8PWK.
360 Accessed 29 Mar 2022.

361 Richardson, A. J., C. Risien and F. A. Shillington (2003), Using self-organizing maps to identify
362 patterns in satellite imagery, *Progress in Oceanography*, Vol. 59, No. 2-3, 223- 239, ISSN 0079-
363 6611.

364 Shambayati, S. (2004), On the Benefits of Short-Term Weather Forecasting for Ka-band (32
365 GHz), *Proceedings IEEE Aerospace Conference*, 3, 1498.

366 Slobin, S. D. (2009), Atmospheric and Environmental Effects, *DSN Telecommunications Link*
367 *Design Handbook*, DSN No. 810-005, Space Link Interfaces, Module 105, Rev. D,
368 http://deepspace.jpl.nasa.gov/dsndocs/810-005/105/105D.pdf

369 Su, H., L. Wu, J. H. Jiang, R. Pai, A. Liu, A. J. Zhai, P. Tavallali and M. DeMaria (2020),
370 Applying Satellite Observations of Tropical Cyclone Internal Structures to Rapid Intensification
371 Forecast with Machine Learning, *Geophys. Res. Lett.*, https://doi.org/10.1029/2020GL089102.

372 Teixeira, J. V., H. Nguyen, D. J. Posselt, H. Su and L. Wu (2021), Using machine learning to
373 model uncertainty for water vapor atmospheric motion vectors, *Atmos. Meas. Tech.*, 14, 1941–
374 1957, https://doi.org/10.5194/amt-14-1941-2021.

375 Yuen, J. H. (Ed.) (1983). Deep Space Telecommunications Systems Engineering. New York:
376 Plenum Press.

377 **List of figures**

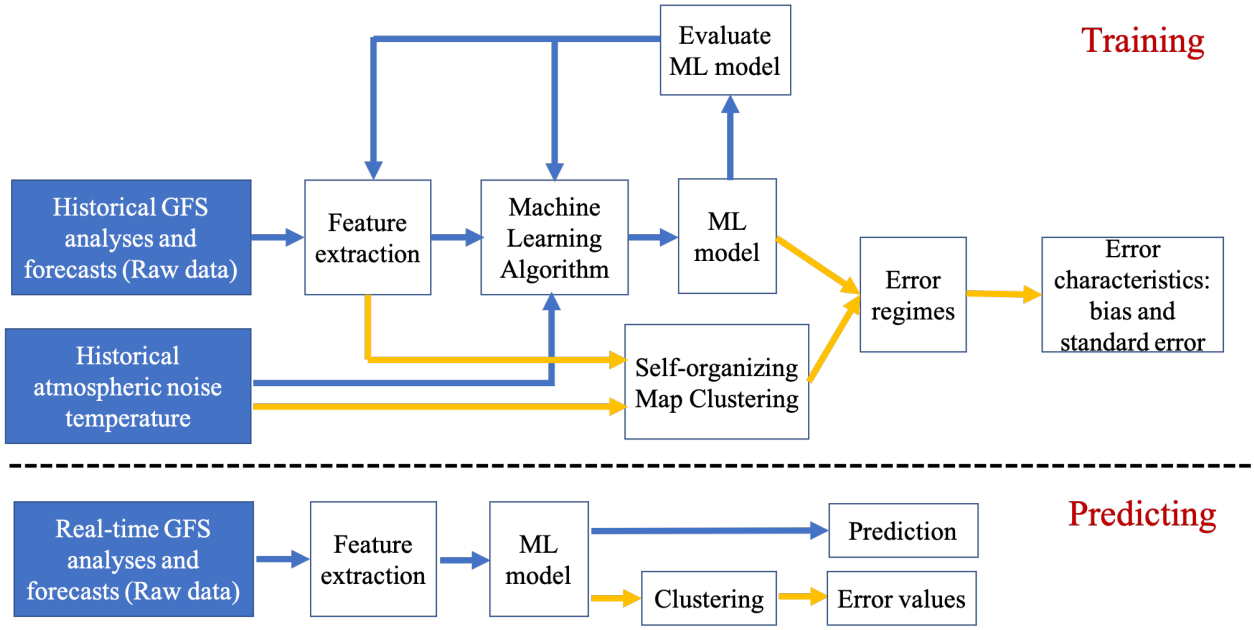

378

379 **Figure 1.** Workflow of the Machine Learning-based forecast system.

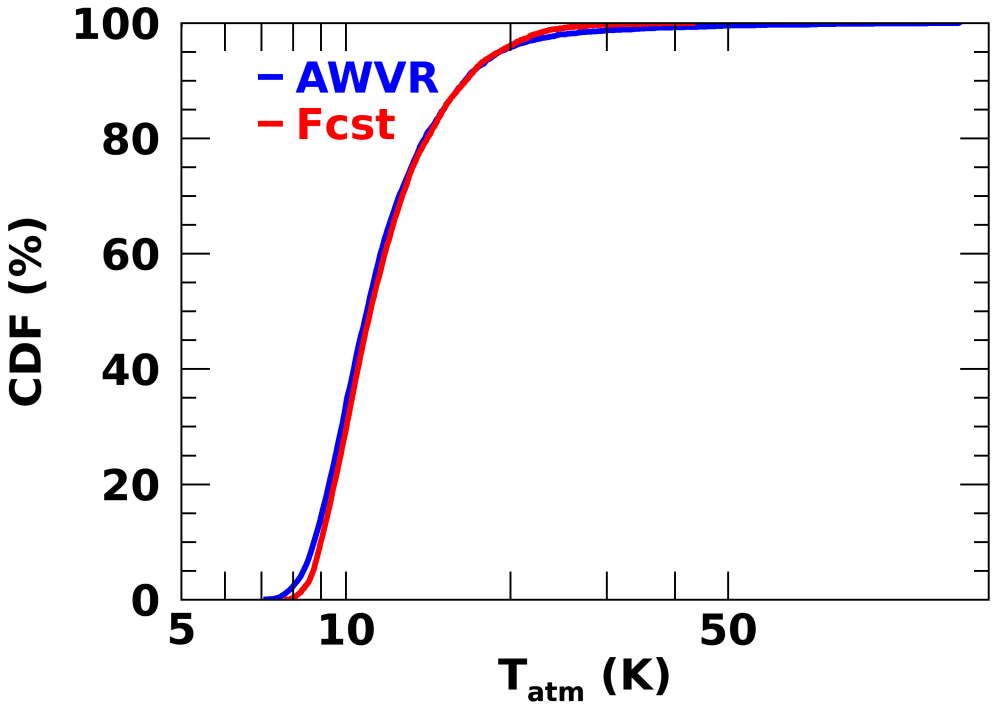

Figure 2. Cumulative distribution function (CDF) of T_{atm} (K) at Goldstone, CA.

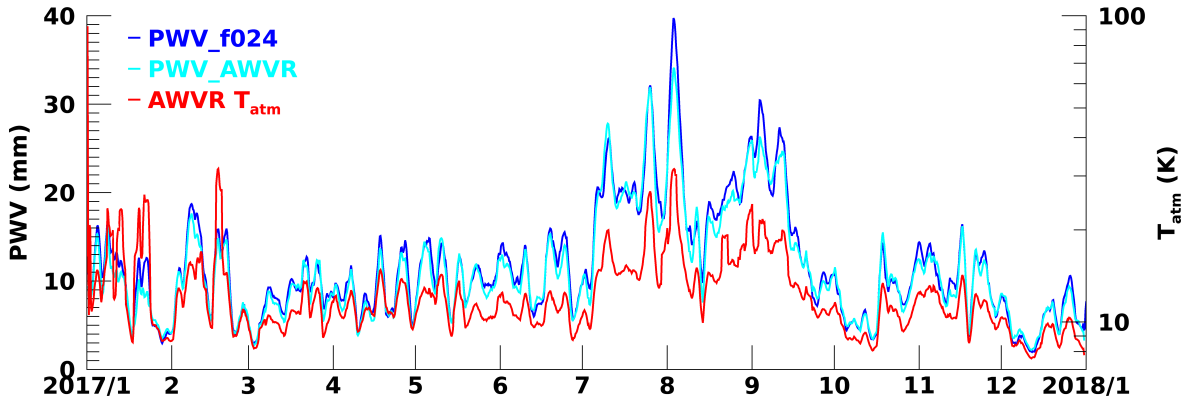

Figure 3. Time series of precipitable water vapor (PWV) from GFS 24-h forecast (PWV_f024) and AWVR measurements (PWV_AWVR), as well as the AWVR T_{atm} in 2017 at Goldstone, CA.

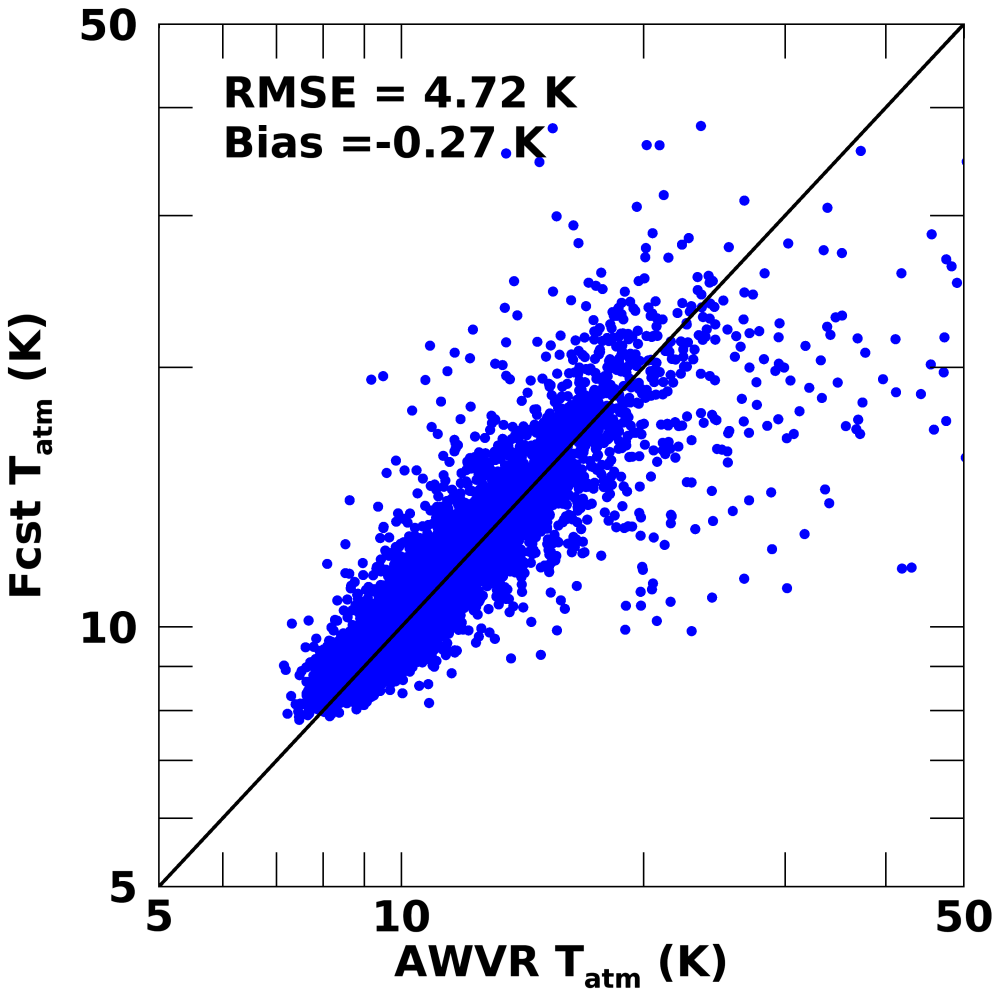

386

387 **Figure 4.** The observed (AWVR) vs. forecasted (Fcst) T_{atm} (K).

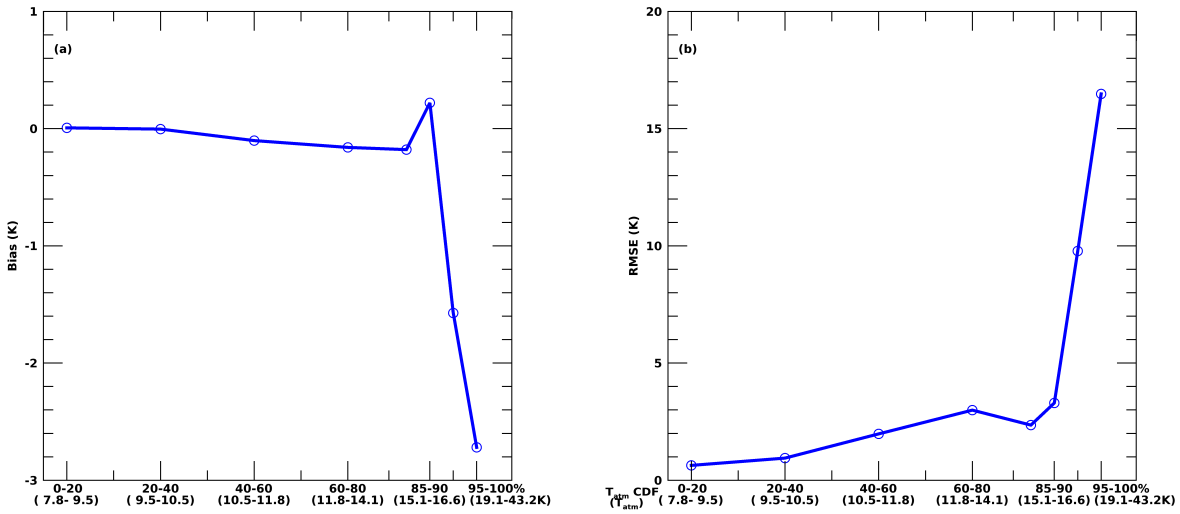

Figure 5. Forecast (a) bias (K) and (b) RMSE (K) sampled by the forecasted T_{atm}. X-axis is the percentile range (%) of the forecasted T_{atm}; values inside parentheses are the corresponding ranges of the forecast T_{atm} (K).

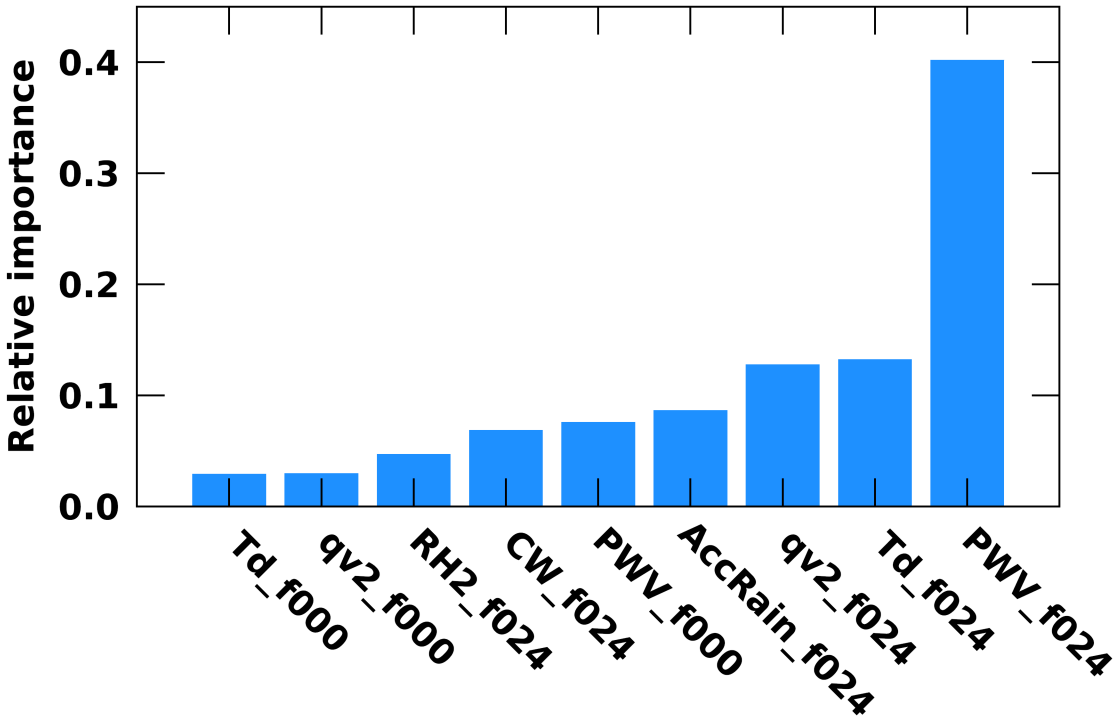

393

394 **Figure 6.** Relative importance of predictors for predicting T_{atm} in 2017 using the ML model.

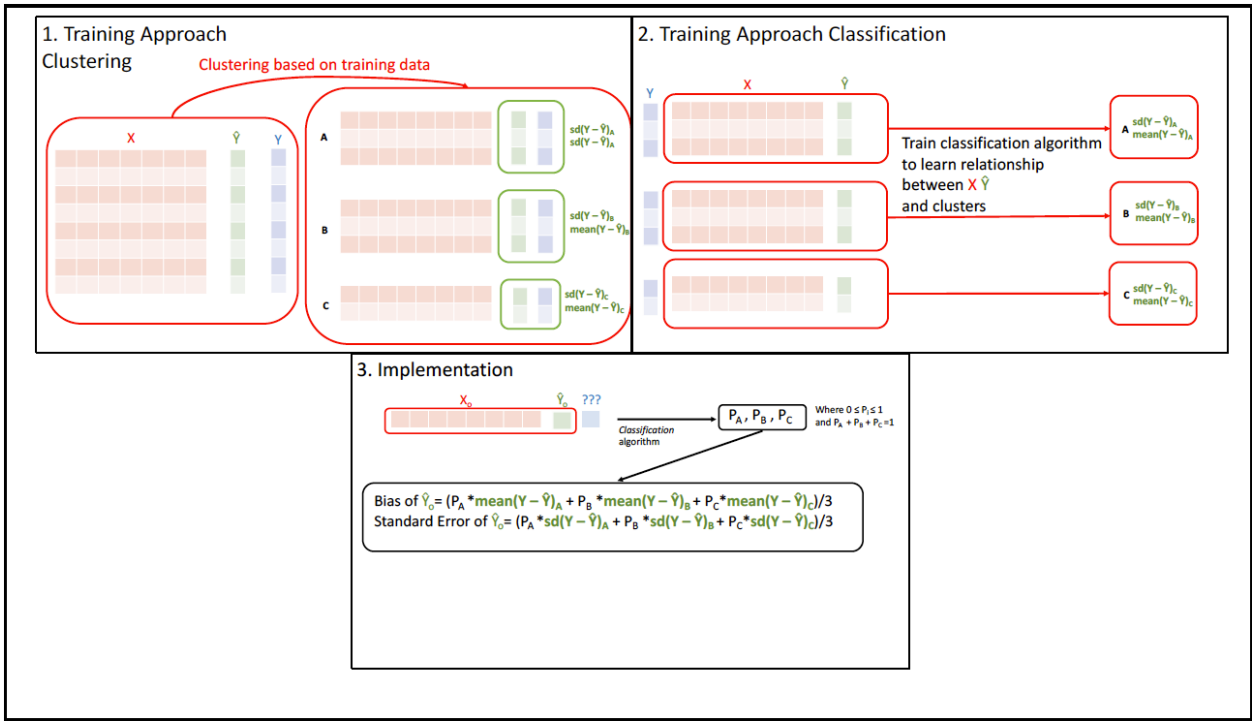

Figure 7. A schematic representation of the Uncertainty Quantification model training and implementation framework. Panel 1 illustrates the clustering step, where a clustering algorithm is trained on the predictors (X), the predict and ($\widehat{Y}$), and the true values (Y). Panel 2 demonstrates the subsequent step, where a classification algorithm models the relationship between X, $\widehat{Y}$, and the defined clusters, circumventing the need for Y in the implementation step (Panel 3).

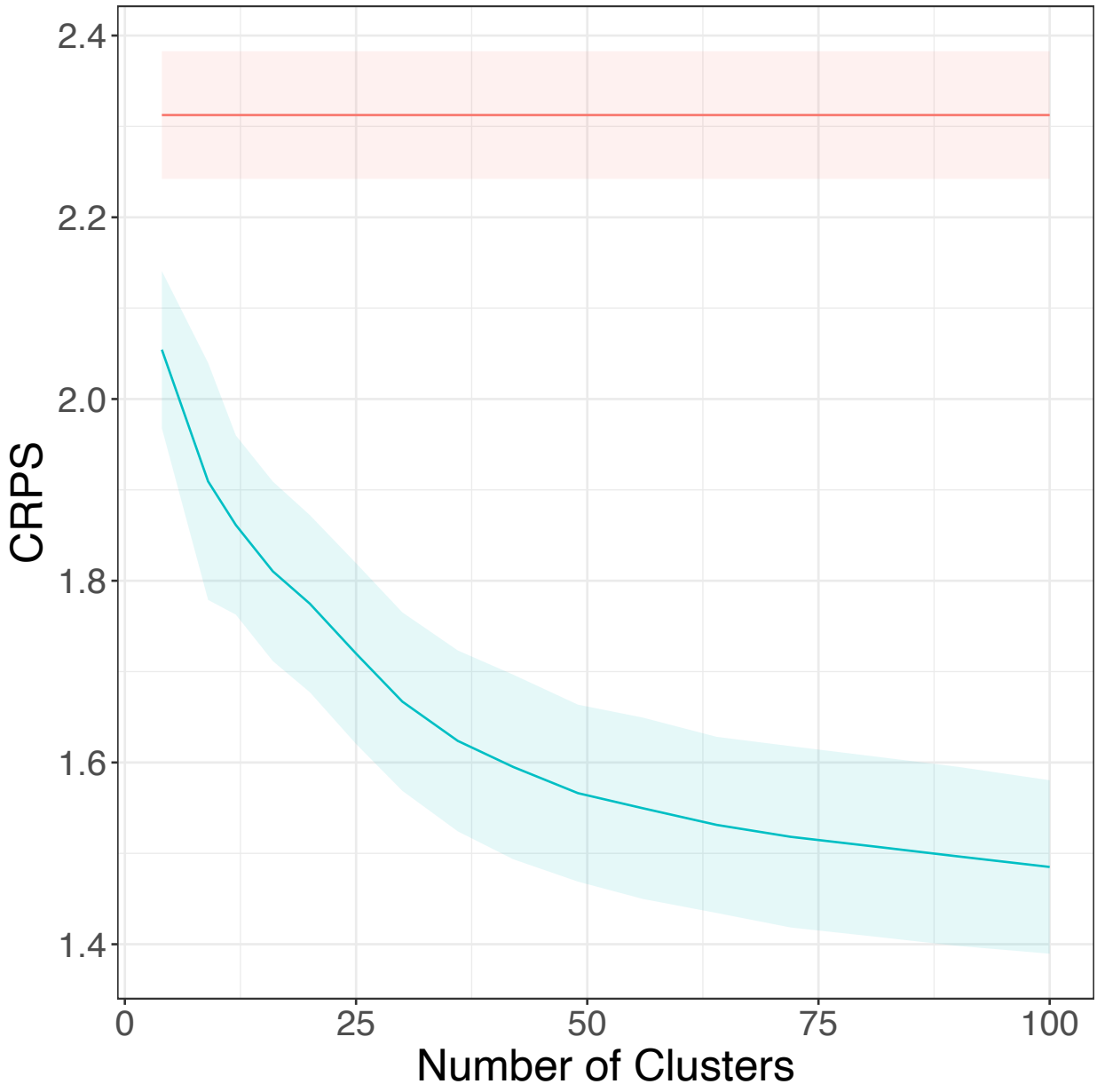

Figure 8. Line plot of CRPS values under different choices of cluster number. The blue line represents the mean CRPS for ensemble predictions at different specified cluster numbers for the Self-Organizing Maps, while the blue shadow area represents the standard deviation of the CRPS for the ensamble. The red line represents the CRPS value for a "naïve" model which considers only the training population mean and standard deviation, with the red shadowed area representing the standard deviation of the CRPS ensamble for different training datasets.

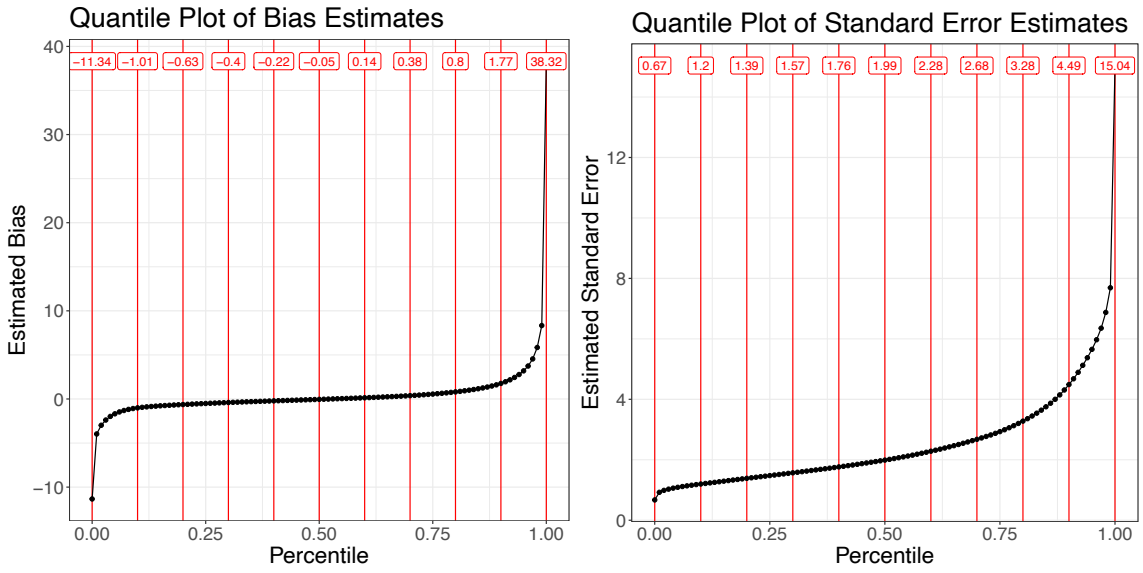

Figure 9. Quantile plot of bias (K) (left panel) and standard error (K) (right panel) from the Uncertainty Quantification model. Each point represents the respective quantile to the nearest one-tenth of a percentile. The red numbers represent the value for each decile (in K), including the maximum and minimum values.

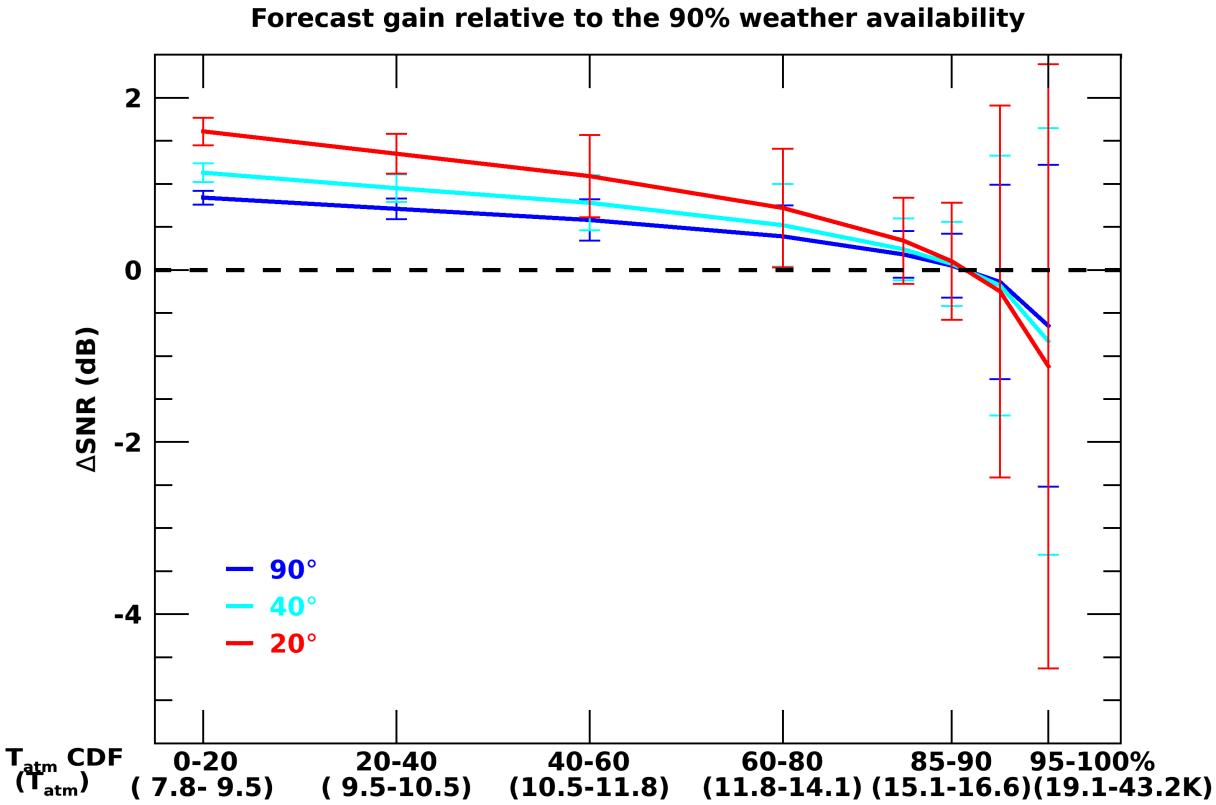

Figure 10. Forecast Gain ($\Delta E_b/N_0$, dB) relative to the 90% weather availability versus mean T_{atm} for different elevation angle cases (90°, 40° and 20°). Error bars represent the forecast errors. X-axis is the percentile range (%) of the forecasted T_{atm}; values inside parentheses are the corresponding ranges of the forecast T_{atm} (K).

List of tables

Table 1. List of predictors to forecast 24-hour T_{atm} in the machine learning forecast model. GFS analysis data is valid at the forecasting time (T0); GFS 24-hour forecast data provides 24-hour forecasts at T0; T_{atm} is valid at 24 hours after the forecasting time (T24). Third Column is the correlation of predictors with $\ln(T_{atm})$.

Variable name	Variable type	Correlation	Description
PWV_f024	24-h forecast	0.71	Precipitable water vapor
qv2_f024	24-h forecast	0.59	2-m specific humidity
Td_f024	24-h forecast	0.57	2-m dew point temperature
PWV_f000	analysis	0.52	Precipitable water vapor
qv2_f000	analysis	0.40	2-m specific humidity
RH2_f024	24-h forecast	0.39	2-m relative humidity
Td_f000	analysis	0.38	2-m dew point temperature
CW_f024	24-h forecast	0.37	Cloud water
AccRain_f024	24-h forecast	0.32	6-hr accumulated precipitation